


 Cite this: *RSC Adv.*, 2026, 16, 15749

# Ultra-sensitive IDE-based ammonia sensor fabricated using green synthesized graphene nanoplatelets and a TiO<sub>2</sub> based composite

 Anita R. Patel,<sup>a</sup> Vishwa Padia,<sup>b</sup> Pruthvi Patel,<sup>a</sup> Dharti Patel,<sup>a</sup> A. K. Dasadia,<sup>b</sup> D. K. Dhruv,<sup>c</sup> Mitesh H. Patel,<sup>d</sup> Shikha Varma<sup>d</sup> and Vanaraj Solanki<sup>\*a</sup>

The development of a reliable, sensitive, and economical gas sensor is crucial for effective environmental monitoring. In this study, we present the development of an interdigitated electrode (IDE) based graphene nanoplatelet (GnP) and GnP-TiO<sub>2</sub> composite NH<sub>3</sub> gas sensor operated at room temperature. Firstly, for the synthesis of GnPs, tea extract was used as a green alternative without the use of organic solvents using a kitchen mixer, whereas TiO<sub>2</sub> and GnP-TiO<sub>2</sub> were prepared *via* a simple hydrothermal process. An IDE-based chemiresistive sensor of GnPs and GnP-TiO<sub>2</sub> was tested for NH<sub>3</sub> detection over a wide concentration range of 100 ppb to 100 ppm at room temperature. The GnP-TiO<sub>2</sub> composite exhibited a response nearly eight times higher than that of the GnP sensor at 100 ppm NH<sub>3</sub>. Additionally, the GnP sensor exhibited response and recovery times of 249 and 107 s, respectively, whereas the GnP-TiO<sub>2</sub> composite achieved 15 and 30 s, corresponding to an ~17 fold faster response time and ~3.5 fold quicker recovery at 100 ppb NH<sub>3</sub>. Overall, this study advocates the applicability of a grown GnP-TiO<sub>2</sub> based composite for NH<sub>3</sub> sensing application in ppb level concentration.

Received 19th January 2026

Accepted 16th March 2026

DOI: 10.1039/d6ra00462h

[rsc.li/rsc-advances](http://rsc.li/rsc-advances)

## 1 Introduction

Numerous hazardous gases and volatile organic compounds such as carbon monoxide (CO), nitrogen dioxide (NO<sub>2</sub>), ammonia (NH<sub>3</sub>), hydrogen (H<sub>2</sub>), methane (CH<sub>4</sub>), toluene, acetone, ethanol, methanol, and benzene are continuously released into the environment due to industrial manufacturing, agricultural activities, and vehicle emissions.<sup>1,2</sup> Ammonia is one of the hazardous gases that can lead to serious health issues or even death when it comes into contact with the eyes, skin, nose, or respiratory system at high concentrations, particularly when NH<sub>3</sub> levels exceed 50 ppm.<sup>3,4</sup> A real-time NH<sub>3</sub> sensor can be effectively used to monitor breath ammonia levels, serving as a non-invasive tool for the diagnosis and monitoring of kidney disorders and ulcers caused by *Helicobacter pylori* bacterial stomach infections.<sup>5,6</sup> Patients with kidney disorders and peptic ulcers exhale NH<sub>3</sub> in the concentration range of 0.82–14.7 ppm.<sup>7</sup> In the presence of moisture, NH<sub>3</sub> can easily react with NO<sub>2</sub> from burning fossil fuels to form ammonium compounds, which are

major contributors to air pollution like Particulate Matter (PM) 2.5.<sup>8</sup> Hence, detecting NH<sub>3</sub> is crucial for safeguarding human health, protecting the environment, and facilitating various medical diagnostic applications.

Gas sensors are categorized based on their detection mechanisms, including chemiresistive, optical, acoustic, thermometric, and gravimetric sensors.<sup>9</sup> Among these, chemiresistive sensors are widely used in gas sensing applications due to their easy fabrication and cost effective processes.<sup>10</sup> A chemiresistive gas sensor's mechanism is based on the adsorption and desorption of target gas molecules onto the surface of sensing material. This interaction alters the charge carrier concentration, leading to a change in resistance. Sensing materials significantly influence gas sensor performance.<sup>11</sup> Amongst different sensing materials, metal oxide semiconductors display better performance due to their exceptional physical and chemical capabilities, as well as their distinctive structural characteristics.<sup>12</sup> Their wide band gap enables tunable semi-conducting behavior, enhancing charge transport and improving gas sensing performance.<sup>13</sup> Based on their electronic nature, metal oxide based gas sensors are generally categorized into n-type and p-type semiconductors in which n-type materials include ZnO,<sup>14</sup> MoO<sub>3</sub>,<sup>15</sup> TiO<sub>2</sub>,<sup>16</sup> and SnO<sub>2</sub> (ref. 17) while NiO<sup>18</sup> and Cu<sub>2</sub>O<sup>19</sup> are commonly known for their p-type behaviour. This classification plays a crucial role in determining their sensing mechanisms and optimizing their performance for specific gas detection applications.<sup>20</sup> Chemiresistive gas sensors based on TiO<sub>2</sub> have gained attention due to their remarkable

<sup>a</sup>Dr. K C Patel R and D Centre, Charotar University of Science and Technology (CHARUSAT), Changa, 388421, Anand, India. E-mail: vanarajsolanki.rnd@charusat.ac.in; miteshpatel.bio@charusat.ac.in

<sup>b</sup>Faculty of Science, A. D. Patel Institute of Technology, The C. V. M University, New Vallabh Vidhyanagar, 388121, Gujarat, India

<sup>c</sup>Natubhai V. Patel College of Pure and Applied Sciences, The Charutar Vidya Mandal (CVM) University, Vallabh Vidyanagar 388120, Gujarat, India

<sup>d</sup>Institute of Physics, Sachivalaya Marg, Bhubaneswar, 751005, India



features, such as reversible and instant changes in electrical resistance, along with exceptional chemical and thermal stability.<sup>21</sup> TiO<sub>2</sub> exist in three phases of like brookite, anatase and rutile, having energy band gap of 2.96, 3.20, and 3.02 eV, respectively. Rutile is the most thermodynamically stable of all these crystal phases. Overall, TiO<sub>2</sub> is a good material for gas sensing, its limitations often require modifications or the use of composites to improve its performance and reliability.<sup>22,23</sup>

Gas sensors that functional at room temperature have received lot of attention of researchers as they consume low power, are simple to integrate, and provide better stability by eliminating the need for high-temperature operation.<sup>24</sup> High-temperature gas sensing provides practical issues, especially when detecting flammable and explosive gases, as the heating element raises the risk of fire.<sup>25</sup> Most metal oxide gas sensors operate at elevated temperatures (200–500 °C) to improve performance, which limits their applications for gas sensing operated at room temperature.<sup>26</sup> To overcome this issue, metal oxide nanostructures are often combined with carbon nanostructures to lower the operating temperature.<sup>27</sup> Nowadays, Graphene and its derivatives have emerged as a highly promising material for applications in nanoelectronics, flexible electronics, sensors, and solar cells. Its exceptional two-dimensional carbon nanostructure offers remarkable properties such as high electrical conductivity, mechanical flexibility, and optical transparency, making it highly versatile for next-generation technologies.<sup>28</sup> However, it suffers from in gas-sensing application due to the poor thermal stability, reduced selectivity, sensitivity to environmental factors like slow response and recovery times, *etc.* Hybridization of graphene allotropes with metal oxides was studied in the literature and it has reported that their hybridized structures show better response as compared to their counterparts.<sup>29–32</sup>

In this study, graphite powder and tea extract were used to synthesize graphene nanoplatelet (GnP) in an economical and environmentally friendly way. The resulting GnP is used as a sensing material for NH<sub>3</sub> sensing. Then, the grown GnP was utilized to synthesize the GnP-TiO<sub>2</sub> composite through a hydrothermal process. The grown material was analyzed to evaluate its morphological, structural, vibrational, and surface chemical characteristics. An interdigitated electrode (IDE) based sensor was developed using GnP and GnP-TiO<sub>2</sub> composite materials for NH<sub>3</sub> detection with a broad concentration range (100 to 100 ppm) at room temperature. In contrast, individual TiO<sub>2</sub> based sensors typically do not operate effectively at room temperature. The GnP-TiO<sub>2</sub> composite sensor exhibited a significantly higher response of 957% compared to 104% for the GnP sensor at 100 ppm NH<sub>3</sub> concentration. This enhanced performance is due to the synergistic effect between GnP and TiO<sub>2</sub>, which improves gas adsorption and charge transfer.

## 2 Experimental

### 2.1 Chemicals

Tea powder was collected from the kitchen (Make by Wagh Bakri Tea Group), graphite powder (Sigma-Aldrich, powder, 100

mesh, <150 μm) was used in this work. Whereas, titanium(IV) butoxide with reagent grade, 97% were acquired from Sigma-Aldrich and hydrochloric acid (HCl) (37% extra pure) was obtained from Loba Chemie Pvt. Ltd. All the reagents used in this experiment were of analytical grade and readily accessible. The kitchen mixer used in this study was made by an Oster, equipped with a 600 W motor.

### 2.2 Synthesis of graphene nanoplatelets

In a typical tea extraction method, 2 g of tea powder is dissolved in 400 mL distilled water at an ambient temperature under constant stirring for 6 h, at a speed of 500 rpm. Substantially, 6 g of graphite powder (*G*) was added to a tea extract and stirred for 3 hours. The solution was shear exfoliated for five minutes using a kitchen mixer. The process was repeated six times to achieve effective exfoliation. The resulting solution was prob sonicated for a duration of 3 h and resultant exfoliated sheets were denoted as a graphene nanoplatelets (GnP) {Fig. 1(a)}.

### 2.3 Synthesis of TiO<sub>2</sub> nanostructures

Titanium(IV) butoxide (3 mL) was added dropwise in an equal volume of HCl and deionised water to synthesize TiO<sub>2</sub> nanostructures. The solution was stirred for 15 minutes to promote homogeneous mixing. The prepared solution was then transferred into a 50 mL Teflon-lined stainless-steel autoclave. The autoclave was heated at 150 °C for 24 hours to facilitate the reaction. Once the reaction was complete, the autoclave was naturally cooled to room temperature. The resulting precipitates were collected by centrifugation at 7000 rpm. In the final step, white powder was then annealed at 550 °C under ambient conditions for 1 hour, leading to the formation of TiO<sub>2</sub> powder.

### 2.4 Synthesis of GnP-TiO<sub>2</sub> nanocomposite

To synthesize GnP-TiO<sub>2</sub> nanocomposite, aforementioned method of TiO<sub>2</sub> deposition was adopted. During the composite deposition, 5 and 10 mL of GnP was additionally added to the precursor solution. The final precipitates were collected and annealed at 500, 600 and 700 °C temperature in air which results in GnP-TiO<sub>2</sub> composite (Fig. 1(b)). Composite grown with 5 ml GnP and annealed at 700 °C temperature was chosen for further study (discussed in the SI S1).

### 2.5 Characterizations

The sample's morphology was examined using scanning electron microscopy (SEM, JEOL 6010LA). The structural analysis of the samples was performed using a D2 Advance X-ray diffractometer (XRD) from Bruker with Cu K<sub>α</sub> radiation ( $\lambda = 1.5418 \text{ \AA}$ ). Diffuse reflectance spectra of TiO<sub>2</sub> and GnP-TiO<sub>2</sub> powders were recorded using a UV-Vis-NIR spectrophotometer (JASCO V-770, Japan) in the wavelength range of 190–2700 nm. Functional group analysis was conducted using Fourier transform infrared (FTIR) spectroscopy with a SHIMADZU IR Spirit-X spectrometer, with a wavenumber range of 400 to 4000 cm<sup>-1</sup>. Raman spectroscopy was carried out using a Renishaw inVia microscope equipped with a 785 nm IR diode laser as the excitation source.



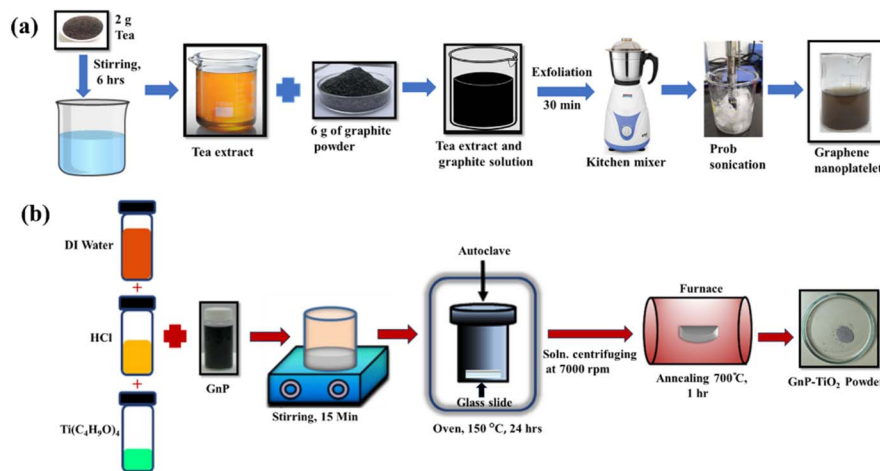


Fig. 1 Schematic synthesis method of (a) GnP, (b) GnP-TiO<sub>2</sub>.

X-ray photoelectron spectroscopy (XPS) analysis was performed using a Thermo Scientific instrument with a monochromated, microfocused Al K $\alpha$  X-ray source ( $h\nu = 1486.6$  eV).

## 2.6 Device fabrications and gas sensing measurements

For device fabrication, a platinum interdigitated (IDE) with dimensions of  $12 \times 20$  mm was first deposited onto a glass substrate, consisting of three pairs of electrodes. The IDE consists of three pairs of electrodes, separated by a gap of 0.8 mm and have a width of 0.4 mm. The sensing materials (GnP, TiO<sub>2</sub> and composites) were then dispersed in water to form a paste, which was hand-printed onto the electrode and dried at 200 °C temperature to make sensing devices. The schematic diagram of the gas sensing setup is presented in the supplementary information (Fig. S1). All gas sensing measurements were carried out at room temperature (RT) inside a test chamber of volume 290 mL. The gas concentrations, of constant flow rate 100 sccm, were regulated using mass flow controllers (MFC). The sensor current was measured using a GAMRY 1010B potentiostat with an applied bias voltage of 0.01 V for GnP and 7 V for GnP-TiO<sub>2</sub> composite based sensor with varying NH<sub>3</sub> concentration in the range from 100 ppb to 100 ppm. To prevent the backflow, during the sensing measurements, a gas exhaust line that ending in a closed water container is used. The chamber was purged using nitrogen gas during sensor recovery cycles. The response,  $R = (I_g/I_0) \times 100\%$ , was defined as the ratio of the current in the gas atmosphere to the current in the air for GnP-TiO<sub>2</sub>, whereas it defined in reverse way for GnP due to its p-type character. The response time is defined as the time taken by the sensor current to rise from 10 to 90% of the total current change during gas adsorption, while the recovery time is defined as the time required for the sensor current to decrease from 90 to 10% during desorption.<sup>33</sup> To ensure reproducibility of the sensing measurements, three independently fabricated GnP-TiO<sub>2</sub> sensors were tested under identical conditions, each subjected to three NH<sub>3</sub> sensing cycles. Statistical analysis was conducted using ANOVA and *T*-test critical at a 95% ( $p > 0.05$ ) confidence level<sup>34</sup> (Tables S1–S3). The results are reported as

mean  $\pm$  standard deviation (SD), and the error bars in the plots correspond to the standard deviation.

## 3 Results and discussion

### 3.1 Morphological study

SEM images of grown nanostructures are shown in Fig. 2. The images of (a) clearly demonstrate the platelet-like morphology of the synthesized GnP nanostructures with an average size of 3.1  $\mu\text{m}$ , as represented in Fig. 2(b). Fig. 2(c) shows SEM images of TiO<sub>2</sub> nanostructures exhibiting uniformly distributed broccoli-like flower morphologies, arise from 7–12 bunches of rod-like nanostructures {inset Fig. 2(c)}. The average diameter of a broccoli flower is about 4.64  $\mu\text{m}$ , as seen in the Fig. 2(d). Fig. 2(e and f) displays the SEM images of the GnP-TiO<sub>2</sub> composite, showing that flower-like TiO<sub>2</sub> nanostructures are anchored onto the sheets of graphene nanoplatelet, resulting in a rough and porous surface morphology of the composite. In some regions, the GnP sheets appear to fold, forming tube-like structures that are decorated with flower-like TiO<sub>2</sub> nanostructures as presented in the inset of Fig. 2(e). This implies strong interaction between GnP and TiO<sub>2</sub>.

### 3.2 Structural study

X-ray diffraction (XRD) is a powerful technique used to determine the crystal structure of materials. The XRD patterns of GnP, TiO<sub>2</sub>, and GnP-TiO<sub>2</sub> are shown in Fig. 3. The most prominent peak observed for GnP is at  $2\theta = 25.71^\circ$ , which is shifted to a lower angle as compared to the graphite peak appeared at  $26.3^\circ$ , due to good exfoliation of graphite {inset of Fig. 3(a)}. An interlayer spacing of 3.46 Å, calculated using (002) plane, is in good agreement with GnP.<sup>35,36</sup> The XRD pattern of TiO<sub>2</sub> displays diffraction peaks at  $2\theta$  values of  $27.50^\circ$ ,  $36.05^\circ$ ,  $39.19^\circ$ ,  $41.16^\circ$ ,  $44.05^\circ$ ,  $54.35^\circ$ ,  $56.64^\circ$ ,  $62.75^\circ$ ,  $64.05^\circ$ ,  $68.93^\circ$ , and  $69.85^\circ$ , which correspond to the (110), (101), (200), (111), (210), (211), (220), (002), (310), (301), and (112) lattice plane respectively as shown in Fig. 3(b). These lattice planes are related to the rutile-phase of TiO<sub>2</sub>, according to JCPDS card no. 88-1175. The strong and



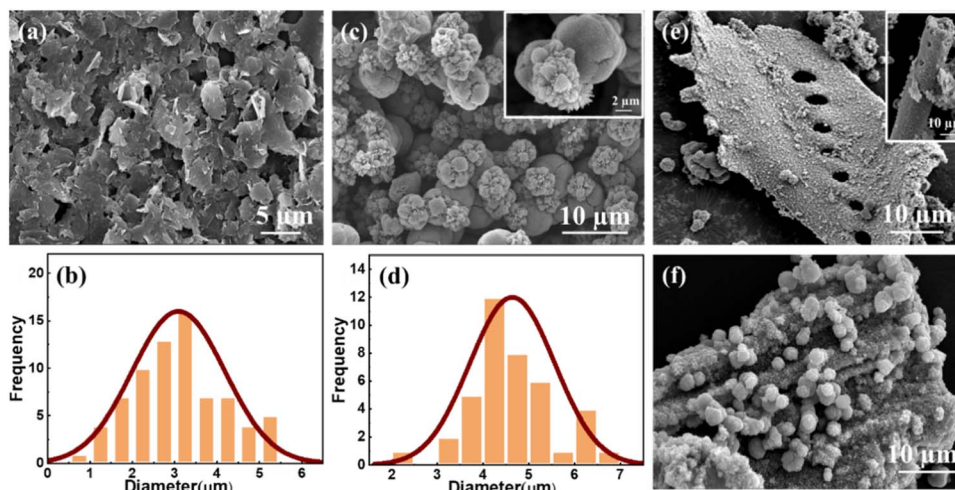


Fig. 2 Morphological analysis (a) SEM image of GnP, (b) histogram of GnP nanostructures, (c) SEM image of TiO<sub>2</sub>, (d) histogram of TiO<sub>2</sub> and (e and f) SEM image of GnP-TiO<sub>2</sub> nanocomposite. Insets show zoomed view for respective nanostructures.

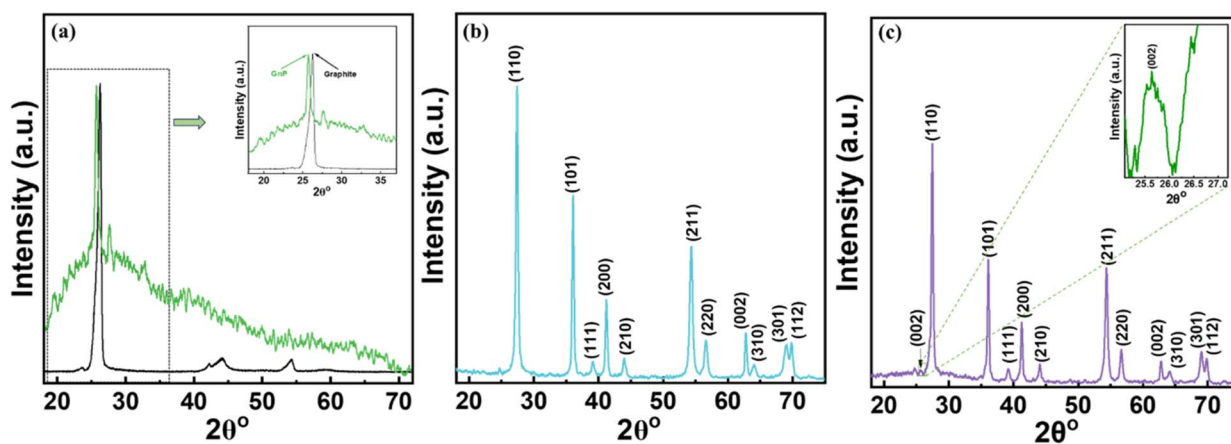


Fig. 3 XRD pattern of (a) GnP, (b) TiO<sub>2</sub> and (c) GnP-TiO<sub>2</sub> nanocomposite.

intense peaks show the high crystallinity of rutile TiO<sub>2</sub> nanostructures.<sup>37,38</sup> In Fig. 3(c), the small peak near 25.71°, corresponds to GnP, showing its effective integration into the composite {inset Fig. 3(c)}. The diffraction peaks of TiO<sub>2</sub> are not affected in the GnP-TiO<sub>2</sub> composite, indicating that the incorporation of graphene nanoplatelets does not alter the crystal structure of TiO<sub>2</sub>. The presence of GnP and rutile TiO<sub>2</sub> related peaks suggests their successful integration.

### 3.3 Optical study

UV-Vis diffuse reflectance spectroscopy was used to analyse the optical characteristics of TiO<sub>2</sub>, and GnP-TiO<sub>2</sub> nanostructures, and the results are presented in Fig. 4. TiO<sub>2</sub> and composite nanostructures both exhibits reflectance edge in the wavelength region of 387 to 393 nm, that associated with its wide bandgap arising from their intrinsic electronic structure.<sup>39</sup> The optical bandgap energies were determined by Kubelka-Munk transformed diffuse reflectance spectra. The optical bandgap of pristine TiO<sub>2</sub> was estimated to be 3.03 eV, while the GnP-TiO<sub>2</sub>

composite shows a slightly higher value of 3.06 eV {Fig. 4(b)}, indicating the incorporation of graphene nanoplatelets does not significantly alter the intrinsic bandgap of TiO<sub>2</sub>.<sup>40</sup> Instead, graphene nanoplatelets act as an efficient charge-transfer network in the composite. Thus, the UV-Vis analysis confirms that graphene nanoplatelets enhance charge-transfer efficiency without intrinsic bandgap modification, which is favourable for gas sensing applications.

### 3.4 Raman study

Fig. 5(a) shows Raman spectrum of GnP, TiO<sub>2</sub> and GnP-TiO<sub>2</sub> nanocomposites. The Raman spectrum of GnP shows D, G, and 2D bands at 1318 cm<sup>-1</sup>, 1584 cm<sup>-1</sup>, and 2632 cm<sup>-1</sup>, respectively.<sup>41</sup> The D band arises due to the sp<sup>3</sup> hybridized carbon atoms and structural defects in GnP, whereas G band corresponds to the E<sub>2g</sub> vibration mode of sp<sup>2</sup> hybridized carbon atoms.<sup>42</sup> The calculated intensity ratio of the D-band to the G-band ( $I_D/I_G$ ) is 0.95, indicating a significant presence of defects in the graphene nanoplatelet.<sup>43</sup> The 2D band, observed



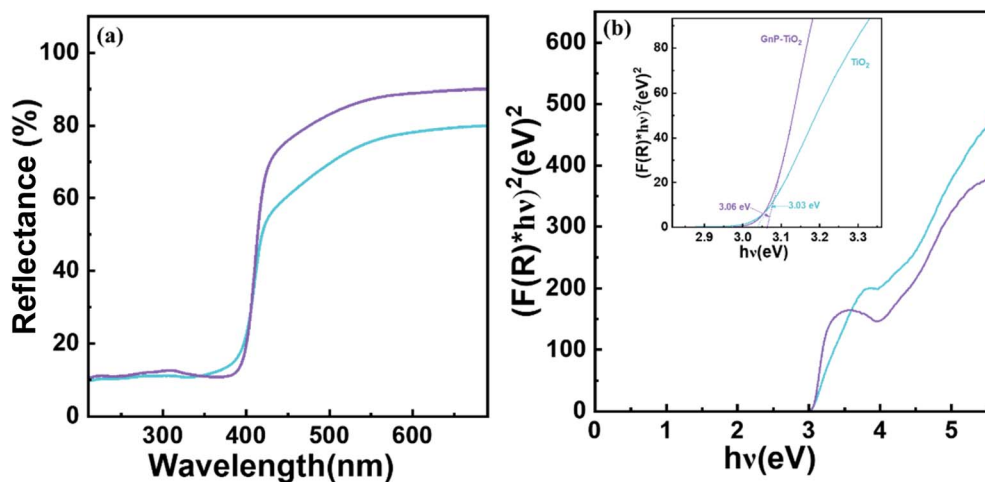


Fig. 4 (a) UV-Vis reflectance spectra (b) Kubelka–Munk plot of  $\text{TiO}_2$  and  $\text{GnP-TiO}_2$  nanocomposite.

at position  $2632\text{ cm}^{-1}$ , indicates the second-order overtone of the D-band. This band is highly sensitive to the number of graphene layers. The GnP grown here consist  $\sim 8$  layers, as calculated from intensity ratio of the 2D band to the G band ( $I_{2D}/I_G$ ) being 0.2053 (ref. 29) Crystallite size was estimated using Tuinstra and Koenig relation, given by,

$$L_a\text{ (nm)} = C(\lambda)/I_D/I_G$$

where  $I_D$  is the intensity of the D peak,  $I_G$  is the intensity of the G peak,  $C(\lambda)$  is the wavelength-dependent prefactor, being 3.5 for the 785 nm laser used here. The calculated crystallite size is  $\sim 3.68\text{ nm}$ .<sup>44</sup> The Raman spectrum of rutile  $\text{TiO}_2$  exhibits characteristic bands at  $142\text{ cm}^{-1}$ ,  $446\text{ cm}^{-1}$ , and  $609\text{ cm}^{-1}$  representing vibrational modes with  $B_{1g}$ ,  $E_g$ , and  $A_{1g}$  symmetry, respectively. The  $B_{1g}$  mode represents oxygen bending motion of  $\text{TiO}_2$ , while the  $E_g$  and  $A_{1g}$  modes arise from symmetric stretching and asymmetric bending of Ti–O bonds. In addition, a characteristic peak observed at  $230\text{ cm}^{-1}$ , arises due to

multiphonon scattering processes.<sup>45</sup> In  $\text{GnP-TiO}_2$  composites, the  $E_g$  mode shifts from  $446\text{ cm}^{-1}$  to  $441\text{ cm}^{-1}$ , while  $B_{1g}$  and  $A_{1g}$  modes retain the same position as compared to pure  $\text{TiO}_2$ , confirming that the rutile phase remains unaffected by GnP incorporation. The multiple Raman phonon scattering shifts from  $230\text{ cm}^{-1}$  in  $\text{TiO}_2$  (ref. 46) to  $236\text{ cm}^{-1}$  in  $\text{GnP-TiO}_2$ . Additionally, in the  $\text{GnP-TiO}_2$  composite, the D band shift from  $1318$  to  $1344\text{ cm}^{-1}$ , the G band shifts from  $1584$  to  $1570\text{ cm}^{-1}$ , and the 2D band shifts from  $2632$  to  $2696\text{ cm}^{-1}$  compared to pure GnP {inset Fig. 5(a)}. Notably, the intensity ratio of the D-band to the G-band is decreases from 0.95 to 0.20 after formation of the  $\text{GnP-TiO}_2$  composite, indicating recovery of the  $sp^2$  carbon domains and improved  $\pi$ - $\pi$  conjugation within the carbon network in the composite formation.<sup>47</sup> The clear modification of GnP and  $\text{TiO}_2$  Raman bands in the composite indicates strong electronic coupling and charge transfer between GnP and  $\text{TiO}_2$ , which plays a dominant role in enhancing the gas-sensing response.<sup>48</sup>

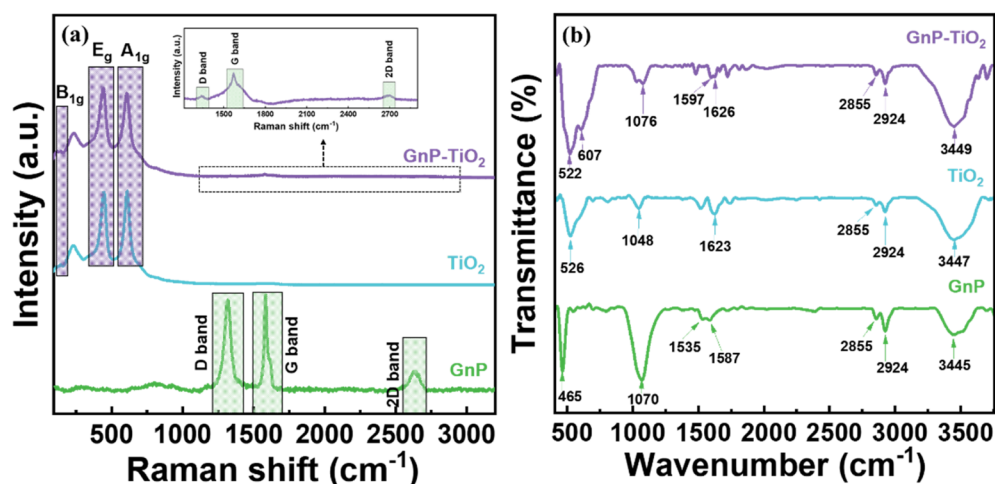


Fig. 5 (a) Raman spectrum (b) FTIR spectrum of GnP,  $\text{TiO}_2$  and  $\text{GnP-TiO}_2$  composite.



### 3.5 FTIR study

The functional groups of the grown GnP, TiO<sub>2</sub>, and GnP-TiO<sub>2</sub> composite were analyzed using FTIR spectroscopy in the wavenumber range of 400 to 4000 cm<sup>-1</sup>, and results are presented in Fig. 5(b). In the FTIR spectrum of GnP, the peak at 3445 cm<sup>-1</sup> is attributed to the O-H stretching vibration of hydroxyl groups along with the peaks at 1535 and 1587 cm<sup>-1</sup> are related to the C=C stretching vibrations of aromatic rings in sp<sup>2</sup> carbon structures.<sup>49–51</sup> In addition, peaks at 1070 and 465 cm<sup>-1</sup> are attributed to C-O-C stretching vibrations that originated from tea extract containing polyphenols, amino acids, and other biomolecules.<sup>52</sup> FTIR spectrum of TiO<sub>2</sub> shows the peak at 526 cm<sup>-1</sup> indicating Ti-O bond vibrations.<sup>53</sup> The absorption band at 1623 cm<sup>-1</sup> is attributed to the bending vibrations of the Ti-OH group, as well as the peak at 3447 cm<sup>-1</sup> attributed to the O-H stretching vibration.<sup>54</sup> In the case of composite material, peaks observed at 522 and 607 cm<sup>-1</sup> correspond to stretching vibrations of Ti-O and Ti-O-Ti bond, respectively. Generally, formation of peaks below 1000 cm<sup>-1</sup> is related to the Ti-O-C bond, whereas the peak at 3449 cm<sup>-1</sup> is attributed to O-H stretching vibrations.<sup>55</sup> In addition, the peaks at 1597 cm<sup>-1</sup> (C=C band),<sup>50</sup> 1076 cm<sup>-1</sup> (C-O-C stretching),<sup>52</sup> and 1626 cm<sup>-1</sup> (Ti-OH bending)<sup>54</sup> are also observed. The peaks at 2855 and 2924 cm<sup>-1</sup> observed are typically attributed to C-H stretching vibrations in GnP, TiO<sub>2</sub>, and their composite.<sup>53,55,56</sup> In the composite of GnP-TiO<sub>2</sub>, the blue shifts observed in the C=C, C-

O-C, and Ti-OH vibrations compared to individual GnP and TiO<sub>2</sub>, and formation of Ti-O-C bond indicate strong interactions between GnP and TiO<sub>2</sub>.

### 3.6 XPS study

The chemical states of the GnP and GnP-TiO<sub>2</sub> composite material are evaluated using XPS and presented in Fig. 6. The survey spectrum of GnP confirms the presence of C and O elements, while the GnP-TiO<sub>2</sub> composite {Fig. 6(a)} shows C, O and Ti peaks. Fig. 6(b) represents the C 1s spectrum of the GnP, revealing four distinct peaks located at 283.8, 284.7, 285.8, and 287.7 eV. The peak at 283.8 is attributed to defect-induced carbon species,<sup>57</sup> while the peak at 284.7 eV corresponds to sp<sup>2</sup>-hybridized C=C bonds, confirming the graphitic carbon.<sup>58</sup> The peak at 285.8 eV is related to oxygenated carbon in the form of C-O or C-O-C, whereas the peak at 287.7 eV is assigned to O-C=O species, indicating the presence of oxidized carbon on the surface of GnP.<sup>59</sup> The O 1s spectrum of graphene nanoplatelets consists of three peaks {Fig. 6(c)} centred at 530.8, 532.2 and 534.7 eV. The Peak at 530.8 eV is attributed to carbonyl (C=O) groups that associated with the presence of defects in GnP. The peaks at 532.2 eV and 534.7 eV are related to C-O-C groups and surface hydroxyl species, respectively.<sup>60,61</sup> The XPS findings are in good agreement with the FTIR results, confirming the presence of C=C, C-O-C, and -OH bands of oxygen-containing functional groups on the GnP surface.

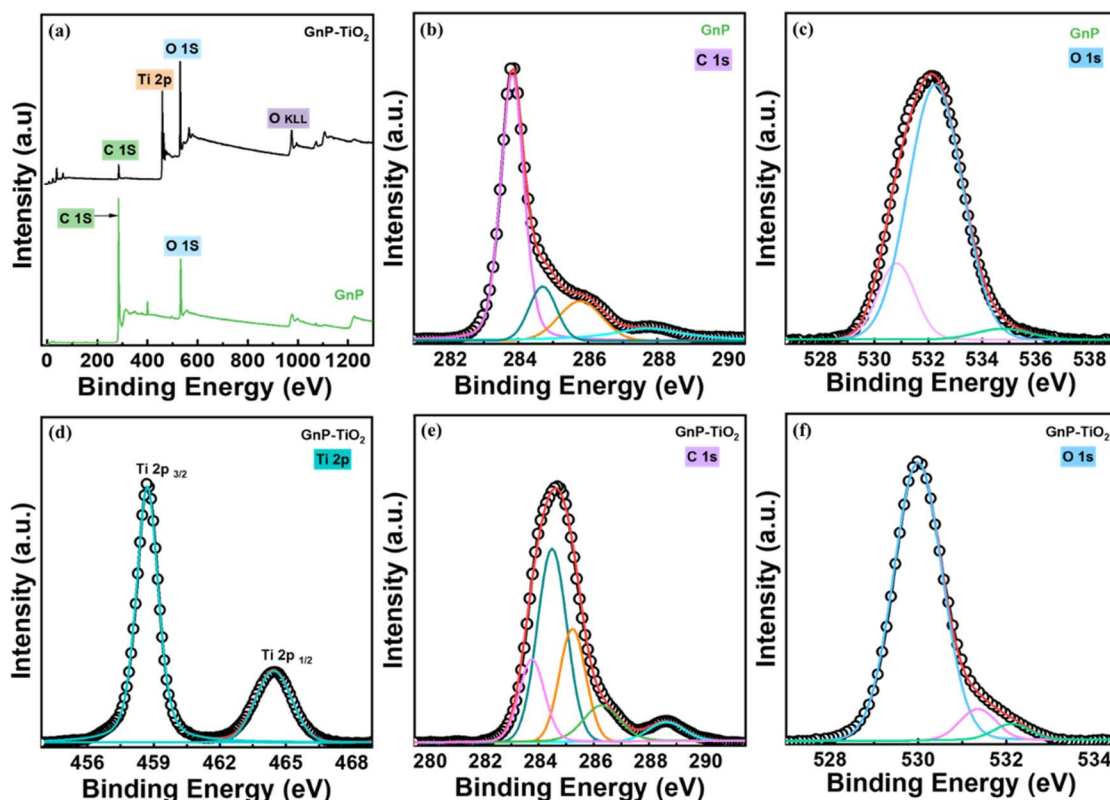


Fig. 6 (a) XPS survey spectrum of GnP and GnP-TiO<sub>2</sub> (b and c) XPS spectra of C and O in GnP (d–f) XPS spectra of Ti, C, and O in GnP-TiO<sub>2</sub> nanocomposite.



Fig. 6(d) shows the Ti 2p spectrum of the composite material, which exhibits two characteristic peaks at 458.7 eV and 464.4 eV, attributed to the Ti 2p<sub>3/2</sub> and Ti 2p<sub>1/2</sub>, respectively, corresponds to Ti<sup>4+</sup> oxidation state in the composite material.<sup>62</sup> Fig. 6(e) represents the C 1s spectrum of the GnP-TiO<sub>2</sub> composite, exhibiting five distinct features located at 283.7, 284.5, 285.2, 286.3, and 288.6 eV. Compared to pristine GnP of C 1s peaks, slight variation in carbon related peaks are observed in the C 1s spectrum of composite. Interestingly, an additional peak related to Ti-O-C interfacial bonding is observed at 286.3 eV, that confirming the chemical bonding between TiO<sub>2</sub> and the surface functional groups of GnP. The O 1s spectrum of the GnP-TiO<sub>2</sub> composite, as shown in Fig. 6(f), exhibits a peak at 529.9 eV, which corresponds to Ti-O-Ti bond.<sup>63</sup> Additionally, the peak at 531.2 and 532 eV are related to Ti-O-C bond and surface hydroxyl group, respectively.<sup>64,65</sup> The presence of Ti-O-C related peak in the XPS spectra of GnP-TiO<sub>2</sub> composite further support the FTIR results and confirm an interaction between GnP and TiO<sub>2</sub>. Furthermore, the formation of Ti-O-C bonds is confirmed by both O 1s and C 1s XPS spectra of the composite and FTIR spectra represents the interfacial bonding that

improves the charge transfer between GnP and TiO<sub>2</sub>, which may contribute to sensing performance.<sup>63</sup>

## 4 Gas sensing properties

A gas sensor for real time applications, it is important to evaluate how the sensor responds in the presence of the target gas. Gas sensing measurements were carried out for all synthesized materials *i.e.* GnP, TiO<sub>2</sub>, and various GnP-TiO<sub>2</sub> based nanostructures. Based on a comparative evaluation, the optimized GnP-TiO<sub>2</sub> (5 mL GnP-TiO<sub>2</sub> annealed at 700 °C temperature) based sensor was selected for detailed gas sensing studies (SI Fig. S1). Fig. 7(a) shows the current response from the GnP based NH<sub>3</sub> sensor for various concentrations ranging from 100 ppb to 100 ppm at room temperature. It is seen that the GnP-based gas sensor exhibits a decrease in current upon exposure to NH<sub>3</sub>, and the current gradually recovers to its initial state after removing NH<sub>3</sub>, representing its recoverable sensing characteristic at lower concentrations. However, the sensor response is not recoverable at NH<sub>3</sub> concentrations of 50 ppm and higher, due to strong adsorption of NH<sub>3</sub> molecules with carbon atoms on the surface. At lower NH<sub>3</sub> concentration of 100

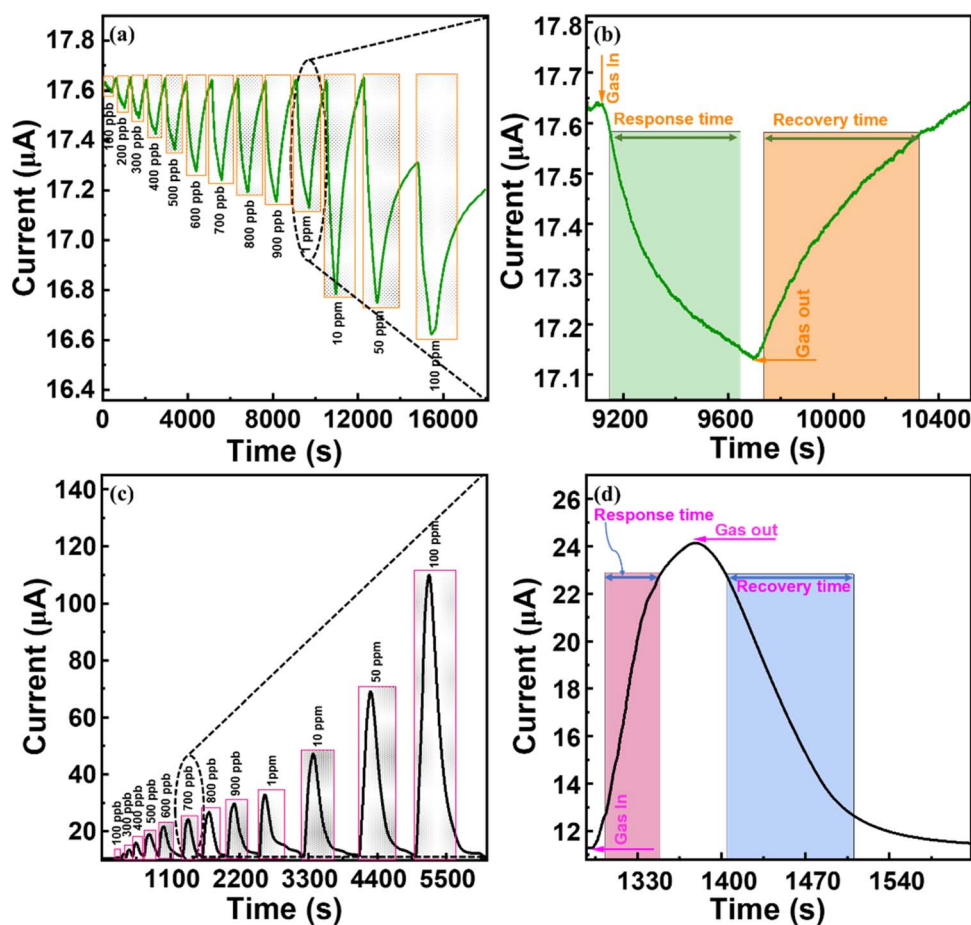


Fig. 7 (a) Current vs. time plot for GnP based sensor for NH<sub>3</sub> gas with different concentrations ranging from 100 ppb to 100 ppm. (b) Zoom view, of (a), to present response and recovery curve for 1 ppm NH<sub>3</sub> concentration. (c) Current vs. time plot for GnP-TiO<sub>2</sub> composite based sensor for NH<sub>3</sub> gas with different concentrations ranging from 100 ppb to 100 ppm. (d) Zoom view, of (c), to show response and recovery curve for 700 ppb NH<sub>3</sub> concentration for GnP-TiO<sub>2</sub> composite.



ppb, the response of the GnP based sensor is 101% which increase with concentration and become 105% for 10 ppm NH<sub>3</sub> concentration. As discussed above  $S$  decrease at higher concentration and become 105 and 104% for 50 and 100 ppm respectively. The dynamic response curve of the GnP sensor, shown in the Fig. 7(b) highlights response and recovery time of 416 and 614 s, respectively, for NH<sub>3</sub> concentration of 1 ppm.

Fig. 7(c) displays the current response of GnP-TiO<sub>2</sub> composite based sensor to NH<sub>3</sub> in the concentration range of 100–100 ppm, at room temperature. The sensor response is fully recoverable here for all range of NH<sub>3</sub> concentrations. The observed response in current is attributed to the adsorption and complete desorption of NH<sub>3</sub> molecules on the sensor surface. Here, response at 100 ppb NH<sub>3</sub> concentration is 105% which increase and become maximum of ~957% for highest concentration of 100 ppm ammonia. The observed response from the composite based sensor is better as compared to pure GnP based sensor. The response and recovery behavior of the GnP-TiO<sub>2</sub> based sensor toward 700 ppb NH<sub>3</sub> is demonstrated in Fig. 7(d) with response and recovery times of 49 s and 106 s, respectively. The observed response and recovery times are smaller for GnP-TiO<sub>2</sub> composite based sensor, as compared to GnP, advocating the superiority of the composite based sensor. In addition, pure TiO<sub>2</sub> based sensor also do not show any response towards NH<sub>3</sub> gas, at room temperature (Fig. S2).

Sensor of real time applications needs to be reproducible and reversible. To check reproducibility and reversibility, the fabricated composite-based sensor was exposed to 5 ppm ammonia concentration and response was recorded for 7 time and demonstrated in Fig. 8(a). This demonstrates that the fabricated sensor exhibits excellent reproducibility and reversibility, as it consistently returns to their initial current across seven repeated NH<sub>3</sub> exposure/removal cycles. GnP based sensor also shows reproducible response towards 1 ppm NH<sub>3</sub> concentration but have poor response (Fig. S3).

To better understand the response behaviour of composite based sensor, the response,  $R$ , is fitted with the Freundlich adsorption isotherm equation  $R = K \times C^\alpha$ , where  $C$  is NH<sub>3</sub> concentration,  $K$  and  $\alpha$  are a proportionality constant and an

exponent, respectively. The value of  $\alpha$  was extracted by plotting  $\log(S)$  versus  $\log(C)$  as shown in Fig. 8(b). For low NH<sub>3</sub> concentration range (100 to 900 ppb), value of  $\alpha$  is 0.42 (black dotted circle) whereas it found to be 0.24 (red dotted circle) for high concentration range (1 ppm to 100 ppm). The high value of  $\alpha$  at low NH<sub>3</sub> concentration indicates the fast and enhanced interaction between available large number of active sites on sensor surface with NH<sub>3</sub> molecules. The observed Ti–O–C bond, observed in FTIR and XPS results, serve as an electron bridge between GnP and TiO<sub>2</sub> in the composite and facilitates an enhanced charge transfer between them. This leads to a steeper and faster response from the composite. At higher ammonia concentration, the value of  $\alpha$  decrease due to lesser number of available active sites on the sensor surface, as compared to lower NH<sub>3</sub> concentration, and result in lower value of exponent. The transition in  $\alpha$ , from high to low value, demonstrates that the sensor response transit from being highly responsive at low concentrations to saturation-limited behavior at higher concentrations of NH<sub>3</sub>.

The stability of the sensors plays a crucial role in long-term functionality and minimizing the need for frequent replacements. The long-term stability of GnP-TiO<sub>2</sub> composite based sensor is presented in Fig. 9(a). To evaluate long-term stability, the sensor was examined for 31 days *via* exposing to 5 ppm NH<sub>3</sub>, and its response was recorded over a period of 31 days. The GnP-TiO<sub>2</sub> composite-based sensor demonstrated excellent stability over 31 days, maintaining a consistent response  $333 \pm 12.89\%$ . This indicates strong durability and consistent sensing performance over time. GnP based sensor also shows good stability towards ammonia gas of 5 ppm concentration with response of  $103 \pm 0.45\%$ , as shown in Fig. S4, but have poor response. The selectivity of the fabricated composite-based sensor was tested towards different gases like ammonia, oxygen, carbon dioxide, nitrogen oxygen, carbon dioxide, nitrogen dioxide *etc.*, at room temperature, and the results are presented in Fig. 9(b). It can be seen that the GnP-TiO<sub>2</sub> sensor response significantly and selectively towards ammonia as compared to other gases {Fig. 9(b)}. Additionally, the limit of detection (LOD) was calculated for both sensors and found to be

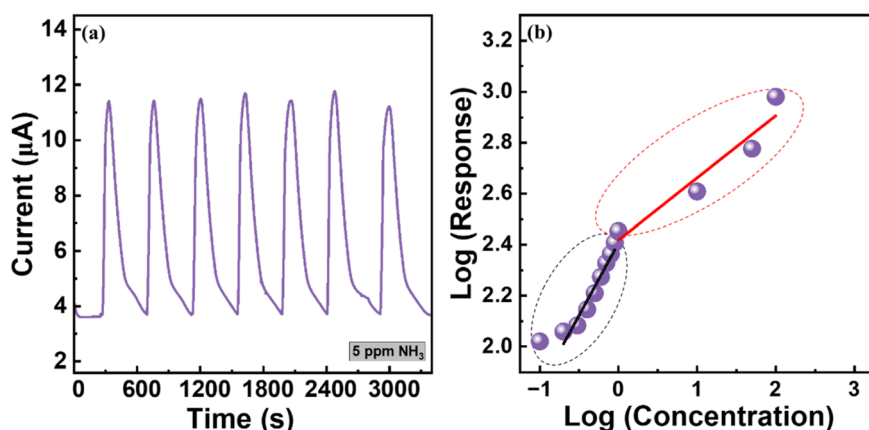


Fig. 8 (a) Repeated cycles for 5 ppm NH<sub>3</sub> gas concentration for GnP-TiO<sub>2</sub> sensor. (b) Log–log plot of response as a function of gas concentration for GnP-TiO<sub>2</sub> composite material.



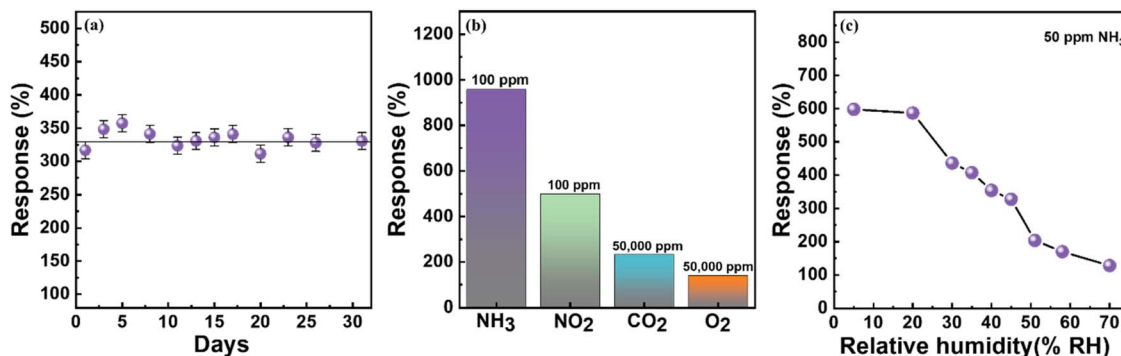


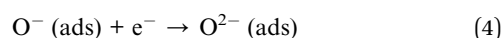
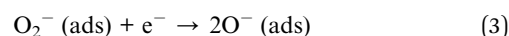
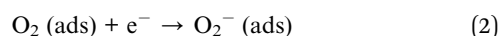
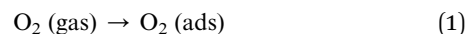
Fig. 9 (a) Long term stability of the GnP-TiO<sub>2</sub> sensor (b) selectivity of the GnP-TiO<sub>2</sub> nanocomposite gas sensor to various gases at room temperature. (c) Effect of different relative humidity on GnP-TiO<sub>2</sub> sensor response.

67 ppb for GnP sensor and 91 ppb for GnP-TiO<sub>2</sub> sensor. The sensitivity of sensors determined to 0.003 and 0.206% per ppb, respectively (Fig. S5).<sup>66</sup> An observed high selectivity from the composite based sensor advocates its capability for real time use. In order to check the effect of humidity on sensor performance, a sensor response as a function of varying humidity was measured from GnP-TiO<sub>2</sub> composite for a constant ammonia concentration of 50 ppm and presented in Fig. 9(c). The relative humidity inside the test chamber was systematically varied between 5 to 70% RH using saturated salt solutions and monitored using a hygrometer. At low relative humid environment, the response variation is negligible being 598% at 5% RH and 587% at 20% RH for 50 ppm NH<sub>3</sub>. The increase of humidity leads to gradual decrease in the sensor response which reaches to ~170% at 70% RH. This behaviour arises as water molecules compete with NH<sub>3</sub> to get adsorb at adsorption sites which then form a thin physisorbed water layer that resists NH<sub>3</sub> adsorption on sensor surface. Additionally, water molecules increase the baseline conductivity through ion formation and cause charge screening in the GnP-TiO<sub>2</sub> material.<sup>67,68</sup> Together, these effects weaken the interaction between NH<sub>3</sub> and the sensor surface, reducing charge transfer and leading to a lower response. Presented results advocate the applicability of fabricated sensor for room temperature ammonia sensing in the sectors that demands monitored environment like medical, corporate office, clean room laboratories *etc.* The sensing performance of the developed GnP/TiO<sub>2</sub> sensor was compared with previously reported NH<sub>3</sub> sensors, as summarized in Table 1.<sup>69–83</sup> W. Saeed *et al.* (2026) reported a Ti<sub>3</sub>C<sub>2</sub>T<sub>x</sub>/SnS<sub>2</sub>/NF based ammonia sensor with a response of 91.7% toward 100 ppm NH<sub>3</sub>, response/recovery times of 42/156 s and a limit of detection of 8.8 ppm.<sup>70</sup> Z. Wu *et al.* reported a high-performance room-temperature NH<sub>3</sub> gas sensor based on Pt-modified WO<sub>3</sub>-TiO<sub>2</sub> nanocrystals synthesized *via* a two-step hydrothermal method. The sensor exhibited a response of approximately 92.28 toward 50 ppm NH<sub>3</sub> with response and recovery times of 23 s and 8 s, respectively, and a limit of detection of 75 ppb.<sup>83</sup> Although this sensor demonstrates a comparatively high sensing response and some studies report faster response and recovery times, the present GnP-TiO<sub>2</sub> composite was synthesized *via* a green synthesis route, without an incorporation of noble metal,

offering an environmentally friendly route. Overall, the combination of high response, ppb-level detection limit, and eco-friendly material synthesis highlights the advancement of the present work compared with previously reported NH<sub>3</sub> sensing devices.

## 5 Gas sensing mechanism

The sensing mechanism of metal oxide (MOX) based gas sensors is generally explained by the space-charge layer model, which involves gas adsorption and interactions between target gas molecules and chemisorbed oxygen species on the sensor surface.<sup>84</sup> The sensing response of MOX materials is classified as n-type or p-type. In conventional n-type oxides (TiO<sub>2</sub>, ZnO, SnO<sub>2</sub>), resistance decreases upon exposure to reducing gases and increases in oxidizing atmospheres, define as a n-type response. p-type MOX exhibits a completely reverse response due to changes in hole carrier concentration. The selective NH<sub>3</sub> sensing performance of the graphene nanoplatelet-TiO<sub>2</sub> composite arises from the synergistic interaction between graphene nanoplatelets and TiO<sub>2</sub>. Furthermore, upon formation of the GnP-TiO<sub>2</sub> heterojunction, electrons transfer from TiO<sub>2</sub> to GnP while holes migrate from GnP to TiO<sub>2</sub> due to the higher Fermi level of TiO<sub>2</sub> relative to GnP. Here, TiO<sub>2</sub> exhibits n-type behaviour, so oxygen molecules from the ambient atmosphere are adsorbed onto its surface and become ionized by capturing electrons from the conduction band, resulting in the formation of reactive oxygen species, including O<sub>2</sub><sup>-</sup>, O<sup>-</sup>, and O<sup>2-</sup>.



The formation of these chemisorbed oxygen ions creates a surface depletion layer at the GnP-TiO<sub>2</sub> interface, as a result resistance of the sensor is high. Upon exposure to NH<sub>3</sub>, it interacts with the chemisorbed oxygen ions on the composite surface, as per the following reaction: {Fig. 10(a)}.<sup>79,85</sup>



Table 1 Comparison of sensing performance of various NH<sub>3</sub> gas sensors

No.	Materials	Ammonia (ppm)	Response	Response time/recovery time	Limit of detection (LOD)	References
1	NiO/ZnO	50	42%	27 s/150 s	—	69
2	Ti <sub>3</sub> C <sub>2</sub> T <sub>x</sub> /SnS <sub>2</sub> /NF	100	91.7%	42 s/156 s	8.8 ppm	70
3	Ti <sub>3</sub> C <sub>2</sub> T <sub>x</sub> /In <sub>2</sub> O <sub>3</sub>	100	146.24%	—	—	71
4	Pd/SnO <sub>2</sub> /RGO	5	7.6%	7 min/50 min	—	72
5	ZnO/rGO	50	3.05%	84 s/216 s	—	73
6	TiO <sub>2</sub> QDs/WS <sub>2</sub>	250	43.72%	—	—	74
7	SnO <sub>2</sub> /rGO	500	190%	8 s/13 s	—	75
8	SnO <sub>2</sub> /SnS <sub>2</sub>	100	248%	21 s/110 s	—	76
9	ZnO/rGO	50	19.2%	50 s/250 s	—	77
10	MWCNT/TiO <sub>2</sub>	500	4.1%	—	—	78
11	Sn-TiO <sub>2</sub> @rGO/CNT	250	85.9%	—	—	79
12	CuO/rGO	50	630%	70 s/112 s	12 ppm	80
13	MOF-derived In <sub>2</sub> O <sub>3</sub> /Co <sub>3</sub> O <sub>4</sub>	10	772%	92 s/51 s	0.5 ppm	81
14	TiO <sub>2</sub> /PANI/GO	100	96%	124 s/102 s	—	82
15	PtNps@TiO <sub>2</sub> -WO <sub>3</sub>	50	92.28	23 s/8 s	75 ppb	83
16	GnP/TiO <sub>2</sub>	100	957%	49 s/106 s	91 ppb	This work



The adsorption of NH<sub>3</sub> on the sensor surface releases electrons into the conduction band of TiO<sub>2</sub>, resulting in a decrease in the thickness of the electron depletion layer in the composite according to the relationship  $R = B \exp(\Delta\Phi q/kT)$  where  $R$  is the sensor resistance,  $B$  is a constant,  $q$  is the electron charge,  $\Delta\Phi$  is

an effective potential barrier height of the p-n heterojunction,  $k$  is Boltzmann's constant, and  $T$  is the temperature of the sensing layer.<sup>86</sup> This will promote the current increase during sensing. Moreover, NH<sub>3</sub> gas sensing of the composite facilitates charge transfer between TiO<sub>2</sub> and NH<sub>3</sub> molecules, which promotes electron transfer through GnP. The experimental results demonstrate that the GnP-based sensor exhibits high electrical conductivity even at low bias voltage, which is attributed to the intrinsically high carrier mobility and low resistivity of graphene nanoplatelets. The incorporation of GnP into the TiO<sub>2</sub> matrix significantly reduces the overall resistance of the composite sensor by providing highly conductive pathways for charge transport. As a result, this composite GnP-TiO<sub>2</sub> sensor operated at room temperature.

Consequently, it is well-known that various gases present in the environment can induce changes in the surface charge state of the sensing material and generate a measurable sensor response, making it difficult to distinguish a specific target gas in mixed-gas conditions. Gas selectivity refers to the ability of a sensor to produce a stronger response to a target gas than to other interfering gases. Nowadays, gas selectivity is a major challenge for gas sensors, and improving selectivity remains an important research focus.<sup>87</sup> As shown in Fig. S6, the GnP-based sensor exhibits a significantly higher response toward NH<sub>3</sub> compared to NO<sub>2</sub>, CO<sub>2</sub>, and O<sub>2</sub>, demonstrating its selective sensing behavior. This indicates that GnP preferentially interacts with reducing gases, particularly NH<sub>3</sub>, as compared to oxidizing gases. This leads to preferential adsorption of NH<sub>3</sub> on the GnP-TiO<sub>2</sub> sensor where the broccoli flower like structures of TiO<sub>2</sub> are randomly entangled with GnP to form a nano-composite network that can provide large active surface area to NH<sub>3</sub> for adsorption during sensing. Furthermore, the form Ti-O-C bonds in this network structure facilitates an enhanced charge transfer in GnP-TiO<sub>2</sub> composite and leads to enhance response as well as selectivity, as shown in Fig. 10(b).<sup>88</sup>

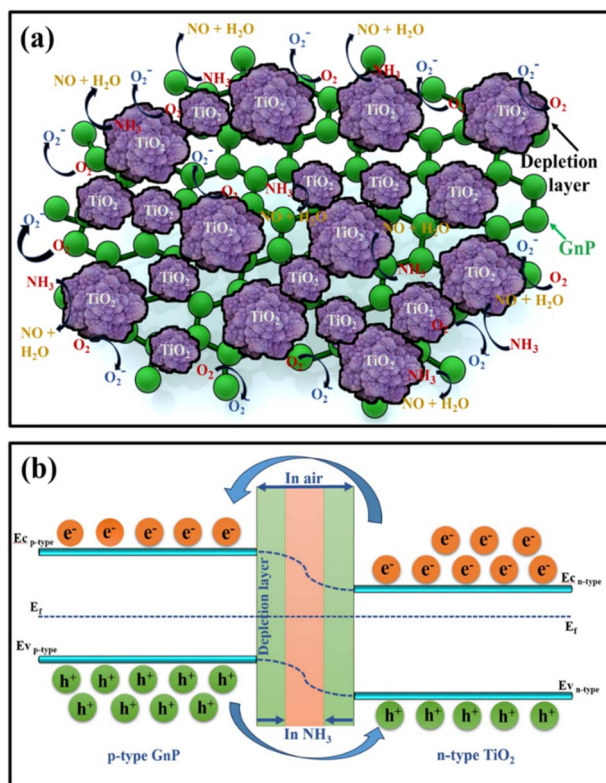


Fig. 10 (a) Schematic diagram of gas sensing mechanism (b) energy band diagram of the heterojunction before and after NH<sub>3</sub> adsorption.



## 6 Conclusions

In conclusion, GnP synthesized using tea extract, along with TiO<sub>2</sub> and its composite, was successfully developed and characterized. The successful formation of GnP, TiO<sub>2</sub>, and GnP decorated with TiO<sub>2</sub> nanostructures was confirmed through SEM, XRD, UV-Vis, FTIR, Raman, and XPS characterizations. Unlike pure TiO<sub>2</sub>, which is inactive at room temperature, the addition of a small fraction of GnP remarkably improved the NH<sub>3</sub> sensing response at room temperature. A GnP-TiO<sub>2</sub> chemiresistive sensor shows a high response of 957% at 100 ppm NH<sub>3</sub> compared to pure GnP nanostructures. In addition, the sensor exhibits outstanding response along with reversible behavior, long-term stability, and strong selectivity towards ammonia. Furthermore, the use of tea extract for GnP synthesis highlights an eco-friendly and sustainable route for fabricating chemiresistive gas sensors. Although the developed GnP-TiO<sub>2</sub> sensor exhibits promising sensing performance toward NH<sub>3</sub>, the further research is needed to lower the operating voltage. In addition, the sensor response decreases with increasing relative humidity due to the competitive adsorption of water molecules on the active sensing sites, which hinders the interaction between the target gas molecules and the sensor surface. Therefore, future studies will focus on the incorporation of suitable dopants or metal nanoparticle modification to increase the electrical and surface properties of the composite, which may help to reduce the operating voltage, improve recovery characteristics, and minimize humidity interference, thereby enhancing the sensor performance under practical environmental conditions. This may be achieved by focusing on improved sensor design and composite structure to enhance sensing performance, particularly to achieve higher sensitivity for ultra-low NH<sub>3</sub> concentrations, potentially reaching the ppt detection range.

## Author contributions

All authors contributed to the study's conception and design. Material preparation, data collection, and analysis were carried out by Anita R. Patel, Vishwa Padia, Pruthvi Patel, Dharti Patel, A. K. Dasadia, D. K. Dhruv, Mitesh H. Patel, Shikha Varma, Vanaraj Solanki. Anita Patel and Vanaraj Solanki wrote the first draft of the manuscript, and all authors reviewed and commented on initial versions. All authors have gone through the manuscript and have approved the same. Anita Patel, Vishwa Padia, Pruthvi Patel, and Dharti Patel: data curation, A. K. Dasadia: conceptualization, and investigation, All authors: formal analysis, D. K. Dhruv and Mitesh H. Patel: visualization, Shikha Varma, Vanaraj Solanki: writing – review, editing, & validation, Vanaraj Solanki and Shikha Varma: project administration, writing – original draft, supervision.

## Conflicts of interest

The authors declare that they have no conflicts of interest.

## Data availability

The data that support the finding of our research are available on reasonable request from the corresponding author.

Supplementary information (SI) is available. See DOI: <https://doi.org/10.1039/d6ra00462h>.

## Acknowledgements

Authors would like to acknowledge Dr. K C Patel R & D Centre, Charotar University of Science and Technology for the experimental facility. Authors are also grateful to Anusandhan National Research Foundation, Department of Science and Technology, Government of India, for Core Research Grant (File Number: CRG/2023/001471). Authors also acknowledge Government of Gujarat for SHODH Fellowship (Reference Number: 202201309).

## References

- 1 L. Kong, X. Tang, J. Zhu, Z. Wang, J. S. Fu, X. Wang, S. Itahashi, K. Yamaji, T. Nagashima, H. J. Lee and C. H. Kim, Evaluation and Uncertainty Investigation of the NO<sub>2</sub>, CO and NH<sub>3</sub> Modeling over China under the Framework of MICS-Asia III, *Atmos. Chem. Phys.*, 2022, **20**, 181, DOI: [10.5194/acp-20-181-2020](https://doi.org/10.5194/acp-20-181-2020).
- 2 T. Lin, X. Lv, Z. Hu, A. Xu and C. Feng, Semiconductor Metal Oxides as Chemoresistive Sensors for Detecting Volatile Organic Compounds, *Sensors*, 2019, **19**, 233, DOI: [10.3390/s19020233](https://doi.org/10.3390/s19020233).
- 3 G. Zhao, J. Xuan, Q. Gong, L. Wang, J. Ren, M. Sun, F. Jia, G. Yin and B. Liu, In Situ Growing Double-Layer TiO<sub>2</sub> Nanorod Arrays on New-Type FTO Electrodes for Low-Concentration NH<sub>3</sub> Detection at Room Temperature, *ACS Appl. Mater. Interfaces*, 2020, **12**(7), 8573, DOI: [10.1021/acsami.9b20337](https://doi.org/10.1021/acsami.9b20337).
- 4 V. Solanki, A. Banerjee and K. K. Nanda, Conductometric room temperature ammonia sensor based on porous tin oxide, *Sens. Actuators, B*, 2022, **366**, 131942, DOI: [10.1016/j.snb.2022.131942](https://doi.org/10.1016/j.snb.2022.131942).
- 5 D. J. Kearney, T. Hubbard and D. Putnam, Breath ammonia measurement in Helicobacter pylori infection, *Dig. Dis. Sci.*, 2002, **47**, 2523, DOI: [10.1023/A:1020568227868](https://doi.org/10.1023/A:1020568227868).
- 6 L. R. Narasimhan, W. Goodman and C. K. N. Patel, Correlation of breath ammonia with blood urea nitrogen and creatinine during hemodialysis, *Proc. Natl. Acad. Sci. U. S. A.*, 2001, **98**, 4617, DOI: [10.1073/pnas.071105798](https://doi.org/10.1073/pnas.071105798).
- 7 H. Y. Li, C. S. Lee, D. H. Kim and J. H. Lee, flexible Room-Temperature NH<sub>3</sub> Sensor for Ultrasensitive, Selective, and Humidity-Independent Gas Detection, *ACS Appl. Mater. Interfaces*, 2018, **10**(33), 27858, DOI: [10.1021/acsami.8b09169](https://doi.org/10.1021/acsami.8b09169).
- 8 S. C. Lee, Y. Cheng, K. F. Ho, J. J. Cao, P. K. K. Louie, J. C. Chow and J. G. Watson, PM1.0 and PM2.5 characteristics in the roadside environment of Hong Kong, *Aerosol Sci. Technol.*, 2006, **40**(3), 157, DOI: [10.1080/02786820500494544](https://doi.org/10.1080/02786820500494544).



- 9 X. Liu, S. Cheng, H. Liu, S. Hu, D. Zhang and H. Ning, A survey on gas sensing technology, *Sensors*, 2012, **12**, 9635, DOI: [10.3390/s120709635](https://doi.org/10.3390/s120709635).
- 10 P. Najafi and A. Ghaemi, Chemiresistor gas sensors: Design, Challenges, and Strategies: A comprehensive review, *Chem. Eng. J.*, 2024, **498**, 154999, DOI: [10.1016/j.cej.2024.154999](https://doi.org/10.1016/j.cej.2024.154999).
- 11 P. Wang, S. Xu, X. Shi, J. Zhu, H. Xiong and H. Wen, Recent Advances in Resistive Gas Sensors: Fundamentals, Material and Device Design, and Intelligent Applications, *Chemosensors*, 2025, **13**(7), 1, DOI: [10.3390/chemosensors13070224](https://doi.org/10.3390/chemosensors13070224).
- 12 V. Solanki, S. B. Krupanidhi and K. K. Nanda, Experimental evidence on RH-dependent crossover from an electronic to protonic conduction with an oscillatory behaviour, *Appl. Phys. Lett.*, 2017, **110**, 263506, DOI: [10.1063/1.4990688](https://doi.org/10.1063/1.4990688).
- 13 F. J. Meng, R. F. Xin and S. X. Li, Metal Oxide Heterostructures for Improving Gas Sensing Properties: A Review, *Materials*, 2023, **16**(1), 263, DOI: [10.3390/ma16010263](https://doi.org/10.3390/ma16010263).
- 14 V. Solanki, D. Kabiraj, D. K. Avasthi and S. Varma, Topographic evolution and scaling study of ZnO (0001) single crystal after low-energy atom beam irradiation, *Nucl. Instrum. Methods Phys. Res., Sect. B*, 2018, **434**, 56, DOI: [10.1016/j.nimb.2018.08.015](https://doi.org/10.1016/j.nimb.2018.08.015).
- 15 F. Ji, X. Ren, X. Zheng, Y. Liu, L. Pang and J. Jiang, 2D-MoO<sub>3</sub> nanosheets for superior gas sensors, *Nanoscales*, 2016, **8**, 8696, DOI: [10.1039/c6nr00880a](https://doi.org/10.1039/c6nr00880a).
- 16 J. Nisar, Z. Topalian, A. Sarkar, L. Osterlund and R. Ahuja, TiO<sub>2</sub>-Based Gas Sensor: A Possible Application to SO<sub>2</sub>, *ACS Appl. Mater. Interfaces*, 2013, **5**(17), 8516–8522, DOI: [10.1021/am4018835](https://doi.org/10.1021/am4018835).
- 17 V. Solanki, S. B. Krupanidhi and K. K. Nanda, Sequential Elemental Dealloying Approach for the Fabrication of Porous Metal Oxides and Chemiresistive Sensors Thereof for Electronic Listening, *ACS Appl. Mater. Interfaces*, 2017, **9**, 41428, DOI: [10.1021/acsami.7b12127](https://doi.org/10.1021/acsami.7b12127).
- 18 M. Valt, M. Caporali, B. Fabbri, A. Gaiardo, E. Iacob, L. Vanzetti, C. Malagu, M. Banchelli, C. D. Andrea, M. Serrano-ruiz, M. Vanni, M. Peruzzini and V. Guidi, Air Stable Nickel-Decorated Black Phosphorus and Its Room-Temperature Chemiresistive Gas Sensor Capabilities, *ACS Appl. Mater. Interfaces*, 2021, **13**(37), 44711–44722, DOI: [10.1021/acsami.1c10763](https://doi.org/10.1021/acsami.1c10763).
- 19 P. Rai, R. Khan, S. Raj, S. M. Majhi, K. Park, Y. Yu, I. Lee and P. K. Sekhar, Au@ Cu<sub>2</sub>O core-shell nanoparticles as Chemiresistors for gas sensor applications : effect of potential barrier modulation on the sensing performance, *Nanoscale*, 2014, **6**, 581, DOI: [10.1039/c3nr04118b](https://doi.org/10.1039/c3nr04118b).
- 20 S. Mahajan and S. Jagtap, Metal-oxide semiconductors for carbon monoxide (CO) gas sensing: A review, *Appl. Mater. Today*, 2020, **18**, 100483, DOI: [10.1016/j.apmt.2019.100483](https://doi.org/10.1016/j.apmt.2019.100483).
- 21 X. Tian, X. Cui, T. Lai, J. Ren, Z. Yang, M. Xiao, B. Wang, X. Xiao and Y. Wang, Gas sensors based on TiO<sub>2</sub> nanostructured materials for the detection of hazardous gases: A review, *Nano Mater. Sci.*, 2021, **3**, 390, DOI: [10.1016/j.nanoms.2021.05.011](https://doi.org/10.1016/j.nanoms.2021.05.011).
- 22 G. W. C. Kumara, H. Hakkoum and E. Comini, Recent Advancements in TiO<sub>2</sub> Nanostructures: Sustainable Synthesis and Gas Sensing, *Nanomaterials*, 2023, **13**(8), 1424, DOI: [10.3390/nano13081424](https://doi.org/10.3390/nano13081424).
- 23 V. Solanki, S. Majumder, I. Mishra, P. Dash, C. Singh and D. Kanjilal, Enhanced anomalous photo-absorption from TiO<sub>2</sub> nanostructures, *J. Appl. Phys.*, 2014, **115**, 184306, DOI: [10.1063/1.4869550](https://doi.org/10.1063/1.4869550).
- 24 P. Srinivasan, M. Ezhilan, A. J. Kulandaisamy, K. J. Babu and J. B. B. Rayappan, Room temperature chemiresistive gas sensors: challenges and strategies—a mini review, *J. Mater. Sci. Mater. Electron.*, 2019, **30**, 15825, DOI: [10.1007/s10854-019-02025-1](https://doi.org/10.1007/s10854-019-02025-1).
- 25 T. Gessner, K. Gottfried, R. Hoffmann, C. Kaufmann, U. Weiss, E. Charetin, P. Hauptmann, R. Lucklum, B. Zimmermann, U. Dietel, G. Springer and M. Vogel, Metal oxide gas sensor for high-temperature applications, *Microsyst. Technol.*, 2000, **6**, 169, DOI: [10.1007/s005420000048](https://doi.org/10.1007/s005420000048).
- 26 V. Galstyan, A. Ponzoni, I. Kholmanov, M. M. Natile, E. Comini, S. Nematov and G. Sberveglieri, Reduced Graphene Oxide-TiO<sub>2</sub> Nanotube Composite: Comprehensive Study for Gas-Sensing Applications, *ACS Appl. Nano Mater.*, 2018, **1**(12), 7098, DOI: [10.1021/acsnm.8b01924](https://doi.org/10.1021/acsnm.8b01924).
- 27 D. Sun, Y. Luo, M. Debligny and C. Zhang, Beilstein, Beilstein, Graphene-enhanced metal oxide gas sensors at room temperature: A review, *J. Nanotechnol.*, 2018, **9**, 2832–2844, DOI: [10.3762/bjnano.9.264](https://doi.org/10.3762/bjnano.9.264).
- 28 A. R. Urade, I. Lahiri and K. S. Suresh, Graphene Properties, Synthesis and Applications: A Review, *J. Miner. Met. Mater. Soc.*, 2023, **75**, 614, DOI: [10.1007/s11837-022-05505-8](https://doi.org/10.1007/s11837-022-05505-8).
- 29 Z. Ismail, N. Farhana, A. Kassim, A. H. Abdullah, A. Sakinah, Z. Abidin, F. S. Ismail and K. Yusoh, Black tea assisted exfoliation using a kitchen mixer allowing one-step production of graphene, *Mater. Res. Express*, 2017, **4**, 075607, DOI: [10.1088/2053-1591/aa7ae2](https://doi.org/10.1088/2053-1591/aa7ae2).
- 30 A. H. Abdullah, Z. Ismail, A. S. Zainal Abidin and K. Yusoh, Green sonochemical synthesis of few-layer graphene in instant coffee, *Mater. Chem. Phys.*, 2019, **222**, 11, DOI: [10.1016/j.matchemphys.2018.09.085](https://doi.org/10.1016/j.matchemphys.2018.09.085).
- 31 D. Zhou, Q. Y. Cheng and B. H. Han, Solvothermal synthesis of homogeneous graphene dispersion with high concentration, *Carbon*, 2011, **49**, 3920–3927, DOI: [10.1016/j.carbon.2011.05.030](https://doi.org/10.1016/j.carbon.2011.05.030).
- 32 Y. Hernandez, V. Nicolosi, M. Lotya, F. M. Blighe, Z. Sun, S. De, I. T. McGovern, B. Holland, M. Byrne, Y. K. Gun'ko, J. J. Boland, P. Niraj, G. Duesberg, S. Krishnamurthy, R. Goodhue, J. Hutchison, V. Scardaci, A. C. Ferrari and J. N. Coleman, High-yield production of graphene by liquid-phase exfoliation of graphite, *Nat. Nanotechnol.*, 2008, **3**, 563, DOI: [10.1038/nnano.2008.215](https://doi.org/10.1038/nnano.2008.215).
- 33 K. G. Krishna, S. Parne, N. Pothukanuri, V. Kathirvelu, S. Gandhi and D. Joshi, Nanostructured metal oxide semiconductor-based gas sensors: A comprehensive review, *Sens. Actuators, A*, 2022, **341**, 113578, DOI: [10.1016/j.sna.2022.113578](https://doi.org/10.1016/j.sna.2022.113578).



- 34 P. Wu, J. Liu, S. Lu, A. Zhang, Y. Tian, J. Xiang, S. Wang and P. Ding, A covalent organic framework/reduced graphene oxide composites-based electrochemical sensing platform for the detection of enrofloxacin, *RSC Adv.*, 2025, **15**, 45333, DOI: [10.1039/d5ra07733h](https://doi.org/10.1039/d5ra07733h).
- 35 A. D. yńska Milena Ojrzyń ska, A. R. Daniewski, K. Wilczyński, J. Jamroz and M. Zdrojek, High-Quality Graphene Nanoplatelets Production with 100% Yield Based on Popular Fertilizer Industry Feedstock, *J. Phys. Chem.*, 2024, **128**, 516, DOI: [10.1021/acs.jpcc.3c06479](https://doi.org/10.1021/acs.jpcc.3c06479).
- 36 D. Shahdan, R. S. Chen and S. Ahmad, Optimization of graphene nanoplatelets dispersion and nano-filler loading in bio-based polymer nanocomposites based on tensile and thermogravimetry analysis, *J. Mater. Res. Technol.*, 2021, **15**, 1284, DOI: [10.1016/j.jmrt.2021.08.130](https://doi.org/10.1016/j.jmrt.2021.08.130).
- 37 R. V. Nair, M. Jijith, V. S. Gummaluri and C. Vijayan, A novel and efficient surfactant-free synthesis of Rutile TiO<sub>2</sub> microflowers with enhanced photocatalytic activity, *Opt. Mater.*, 2016, **55**, 38, DOI: [10.1016/j.optmat.2016.03.015](https://doi.org/10.1016/j.optmat.2016.03.015).
- 38 H. S. Ramadan, R. A. M. Ali, M. Mobarak, M. Badawi, A. Q. Selim, E. A. Mohamed, A. Bonilla-Petriciolet and M. K. Seliem, One-step fabrication of a new outstanding rutile TiO<sub>2</sub> nanoparticles/anthracite adsorbent: Modeling and physicochemical interpretations for malachite green removal, *Chem. Eng. J.*, 2021, **426**, 1, DOI: [10.1016/j.cej.2021.131890](https://doi.org/10.1016/j.cej.2021.131890).
- 39 Q. Huang, S. Tian, D. Zeng, X. Wang, W. Song, Y. Li, W. Xiao and C. Xie, Enhanced photocatalytic activity of chemically bonded TiO<sub>2</sub>/graphene composites based on the effective interfacial charge transfer through the C-Ti bond, *ACS Catal.*, 2013, **3**, 1477, DOI: [10.1021/cs400080w](https://doi.org/10.1021/cs400080w).
- 40 M. Aleksandrak, P. Adamski, W. Kukułka, B. Zielinska and E. Mijowska, Effect of graphene thickness on photocatalytic activity of TiO<sub>2</sub>-graphene nanocomposites, *Appl. Surf. Sci.*, 2015, **331**, 193–199, DOI: [10.1016/j.apsusc.2015.01.070](https://doi.org/10.1016/j.apsusc.2015.01.070).
- 41 H. M. Albetran, Structural Characterization of Graphite Nanoplatelets Synthesized from Graphite Flakes, *Preprints*, 2020, DOI: [10.20944/preprints202008.0325.v1](https://doi.org/10.20944/preprints202008.0325.v1).
- 42 M. A. Pimenta, G. Dresselhaus, M. S. Dresselhaus, L. G. Cançado, A. Jorio and R. Saito, Studying disorder in graphite-based systems by Raman spectroscopy, *Phys. Chem. Chem. Phys.*, 2007, **9**, 1276, DOI: [10.1039/b613962k](https://doi.org/10.1039/b613962k).
- 43 P. Manafi, I. Ghasemi, M. Karrabi, H. Azizi and P. Ehsaninamin, Effect of graphene nanoplatelets on crystallization kinetics of poly (lactic acid), *Soft Mater.*, 2014, **12**, 433, DOI: [10.1080/1539445X.2014.959598](https://doi.org/10.1080/1539445X.2014.959598).
- 44 K. Krishnamoorthy, M. Veerapandian, R. Mohan and S. J. Kim, Investigation of Raman and photoluminescence studies of reduced graphene oxide sheets, *Appl. Phys. A: Mater. Sci. Process.*, 2012, **106**, 501, DOI: [10.1007/s00339-011-6720-6](https://doi.org/10.1007/s00339-011-6720-6).
- 45 E. J. Ekoi, A. Gowen, R. Dorrepaal and D. P. Dowling, Characterisation of titanium oxide layers using Raman spectroscopy and optical profilometry: Influence of oxide properties, *Results Phys.*, 2019, **12**, 1574, DOI: [10.1016/j.rinp.2019.01.054](https://doi.org/10.1016/j.rinp.2019.01.054).
- 46 S. Challagulla, K. Tarafder, R. Ganesan and S. Roy, Structure sensitive photocatalytic reduction of nitroarenes over TiO<sub>2</sub>, *Sci. Rep.*, 2017, **1**, 8783, DOI: [10.1038/s41598-017-08599-2](https://doi.org/10.1038/s41598-017-08599-2).
- 47 Qi. Zhang, N. Bao, X. Wang, Xi. Hu, X. Miao, M. Chaker and Do. Ma, Advanced Fabrication of Chemically Bonded Graphene/TiO<sub>2</sub> Continuous Fibers with Enhanced Broadband Photocatalytic Properties and Involved Mechanisms Exploration, *Sci. Rep.*, 2016, **6**(1), 38066, DOI: [10.1038/srep38066](https://doi.org/10.1038/srep38066).
- 48 E. Lee, D. Lee, J. Yoon, Y. Yin, Y. N. Lee, S. Uprety, Y. S. Yoon and D. J. Kim, Enhanced Gas-Sensing Performance of GO/TiO<sub>2</sub> Composite by Photocatalysis, *Sensors*, 2018, **18**(10), 3334, DOI: [10.3390/s18103334](https://doi.org/10.3390/s18103334).
- 49 S. Rajakumari, S. Mohandoss and S. Sureshkumar, Synthesis and characterization of Cu-rGO/ZnO nanocomposite for photocatalytic degradation of bromophenol blue and antibacterial activity, *J. Chem. Eng.*, 2024, **41**, 1345, DOI: [10.1007/s43153-023-00406-y](https://doi.org/10.1007/s43153-023-00406-y).
- 50 N. Kumar and V. C. Srivastava, Simple Synthesis of Large Graphene Oxide Sheets via Electrochemical Method Coupled with Oxidation Process, *ACS Omega*, 2018, **3**(8), 10233, DOI: [10.1021/acsomega.8b01283](https://doi.org/10.1021/acsomega.8b01283).
- 51 Y. Wang, J. Liu, L. Liu and D. D. Sun, High-quality reduced graphene oxide-nanocrystalline platinum hybrid materials prepared by simultaneous co-reduction of graphene oxide and chloroplatinic acid, *Nanoscale Res. Lett.*, 2011, **6**, 241, DOI: [10.1186/1556-276X-6-241](https://doi.org/10.1186/1556-276X-6-241).
- 52 H. Zhang, X. Wang, N. Li, J. Xia, Q. Meng, J. Ding and J. Lu, Synthesis and characterization of TiO<sub>2</sub>/graphene oxide nanocomposites for photoreduction of heavy metal ions in reverse osmosis concentrate, *RSC Adv.*, 2018, **8**, 34241, DOI: [10.1039/C8RA06681G](https://doi.org/10.1039/C8RA06681G).
- 53 M. S. Johnson, M. Ates, Z. Arslan, I. O. Farah and C. Bogatu, Assessment of Crystal Morphology on Uptake, Particle Dissolution, and Toxicity of Nanoscale Titanium Dioxide on Artemia Salina, *J. Nanotoxicol. Nanomed.*, 2017, **2**, 11, DOI: [10.4018/JNN.2017010102](https://doi.org/10.4018/JNN.2017010102).
- 54 A. León, P. Reuquen, C. Garín, R. Segura, P. Vargas, P. Zapata and P. A. Orihuela, FTIR and Raman Characterization of TiO<sub>2</sub> Nanoparticles Coated with Polyethylene Glycol as Carrier for 2-Methoxyestradiol, *Appl. Sci.*, 2017, **7**(1), 49, DOI: [10.3390/app7010049](https://doi.org/10.3390/app7010049).
- 55 M. Ruid, A. Á. Miguel, G. Cruz-quesada, J. Rivera-utrilla and S. Manuel, Hydrothermal Synthesis of rGO-TiO<sub>2</sub> Composites as High-Performance UV Photocatalysts for Ethylparaben Degradation, *J. Catal.*, 2020, **10**, 520, DOI: [10.3390/catal10050520](https://doi.org/10.3390/catal10050520).
- 56 S. A. Balsamo, R. Fiorenza, M. Condorelli, R. Pecoraro, M. V. Brundo, F. Lo Presti and S. Sciré, One - pot synthesis of TiO<sub>2</sub> -Rgo Photocatalysts for the Degradation of Groundwater Pollutants, *Materials*, 2021, **14**(20), 5938, DOI: [10.3390/ma14205938](https://doi.org/10.3390/ma14205938).
- 57 M. Scardamaglia, T. Susi, C. Struzzi, R. Snyders, G. D. Santo, L. Petaccia and C. Bittencourt, Spectroscopic observation of oxygen dissociation on nitrogen-doped graphene, *Sci. Rep.*, 2017, **7**, 7960, DOI: [10.1038/s41598-017-08651-1](https://doi.org/10.1038/s41598-017-08651-1).



- 58 V. Shukla, Observation of critical magnetic behavior in 2D carbon based composites, *Nanoscale Adv.*, 2020, 2, 962, DOI: [10.1039/C9NA00663J](https://doi.org/10.1039/C9NA00663J).
- 59 Z. Ndala, N. Shumbula, S. Tsoeu, T. Majola, S. Gqoba, C. Langaniso, Z. Tetana and N. Moloto, Enhanced electrocatalytic hydrogen evolution *via* nitrogen-induced electron density modulation in ReSe<sub>2</sub>/2D carbon heterostructures, *RSC Adv.*, 2025, 15, 14200, DOI: [10.1039/D5RA01096A](https://doi.org/10.1039/D5RA01096A).
- 60 S. Gutić, A. S. Dobrota, N. Gavrilov, M. Baljović, I. A. Pašti and S. V. Mentus, Surface Charge Storage Properties of Selected Graphene Samples in pH-neutral Aqueous Solutions of Alkali Metal Chlorides - Particularities and Universalities, *Int. J. Electrochem. Sci.*, 2016, 11, 8662–8682, DOI: [10.20964/2016.10.47](https://doi.org/10.20964/2016.10.47).
- 61 J. V. Rojas, M. Toro-Gonzalez, M. C. Molina-Higgins and C. E. Castano, Facile radiolytic synthesis of ruthenium nanoparticles on graphene oxide and carbon nanotubes, *Mater. Sci. Eng., B*, 2016, 205, 28–35, DOI: [10.1016/j.mseb.2015.12.005](https://doi.org/10.1016/j.mseb.2015.12.005).
- 62 M. S. A. Sher Shah, A. R. Park, K. Zhang, J. H. Park and P. J. Yoo, Green synthesis of biphasic TiO<sub>2</sub>-reduced graphene oxide nanocomposites with highly enhanced photocatalytic activity, *ACS Appl. Mater. Interfaces*, 2012, 4(8), 3893, DOI: [10.1021/am301287m](https://doi.org/10.1021/am301287m).
- 63 U. Nakhikham, V. Boffa, G. Magnacca, A. Qiao, L. R. Jensen and Yu. Yue, Mutual-stabilization in chemically bonded graphene oxide–TiO<sub>2</sub> heterostructures synthesized by a sol–gel approach, *RSC Adv.*, 2017, 7, 41217, DOI: [10.1039/C7RA07472G](https://doi.org/10.1039/C7RA07472G).
- 64 A. Nasir, S. Khalid, T. Yasin and A. Mazare, A Review on the Progress and Future of TiO<sub>2</sub>/Graphene Photocatalysts, *Energies*, 2022, 15(17), 6248, DOI: [10.3390/en15176248](https://doi.org/10.3390/en15176248).
- 65 J. Rodriguez Hueso, R. Ponce-Perez, D. M. Hoat, M. H. Farias, H. Tiznado, S. A. Aguila, H. A. Borbon-Nuñez and J. Guerrero-Sánchez, Atomic layer deposition of TiO<sub>2</sub> on hydroxylated graphene *via* TDMAT: An experimental and theoretical study of nanohybrid nucleation, *Surf. Interfaces*, 2025, 72, 107195, DOI: [10.1016/j.surfin.2025.107195](https://doi.org/10.1016/j.surfin.2025.107195).
- 66 V. S. Choudhary, R. Singh, A. Kumar, C. S. Yadav, S. Sharma, J. Garcia and S. K. Sharma, MoSe<sub>2</sub>-based room temperature gas sensor with a sub-parts-per-billion limit for ammonia and N,N-dimethylformamide, *Mater. Adv.*, 2025, 6, 2854, DOI: [10.1039/D4MA01169D](https://doi.org/10.1039/D4MA01169D).
- 67 N. M. Hieu, C. V. Phuoc, T. T. Hien, N. D. Chinh, N. D. Quang, C. Kim, J. R. Jeong and D. Kim, A Separated Receptor/Transducer Scheme as Strategy to Enhance the Gas Sensing Performance Using Hematite–Carbon Nanotube Composite, *Sensors*, 2019, 19(18), 3915, DOI: [10.3390/s19183915](https://doi.org/10.3390/s19183915).
- 68 L. Yao, X. Tian, X. Cui, R. Zhao, X. Xiao and Y. Wang, Partially oxidized Ti<sub>3</sub>C<sub>2</sub>T<sub>x</sub> MXene-sensitive material-based ammonia gas sensor with high-sensing performances for room temperature application, *J. Mater. Sci.: Mater. Electron.*, 2021, 32, 27837–27848, DOI: [10.1007/s10854-021-07166-w](https://doi.org/10.1007/s10854-021-07166-w).
- 69 J. Wang, P. Yang and X. Wei, High-performance, room-temperature, and no-humidity-impact ammonia sensor based on heterogeneous nickel oxide and zinc oxide nanocrystals, *ACS Appl. Mater. Interfaces*, 2015, 7(6), 3816, DOI: [10.1021/am508807a](https://doi.org/10.1021/am508807a).
- 70 W. Saeed, Y. Tian, I. A. Mir, B. Miao, A. Manzoor, S. Rana and X. Chen, Comparative analysis of Nafion-functionalized few-layered *vs.* multilayered Ti<sub>3</sub>C<sub>2</sub>T<sub>x</sub> MXene/SnS<sub>2</sub> nanoflowers for ammonia detection with enhanced selectivity, *RSC Adv.*, 2026, 16, 12165, DOI: [10.1039/D6RA00396F](https://doi.org/10.1039/D6RA00396F).
- 71 J. Zhang, S. Wang, R. Yang, J. Liu, X. Zhang, W. Yu, T. Xu, J. Guo, X. Zhang, J. Gao and H. Lu, Ti<sub>3</sub>C<sub>2</sub>T<sub>x</sub>/In<sub>2</sub>O<sub>3</sub> heterojunction nanocomposite-based flexible sensor for selective detection of NH<sub>3</sub> at room temperature, *J. Mater. Sci. Mater. Electron.*, 2015, 36, 1003, DOI: [10.1007/s10854-025-15113-2](https://doi.org/10.1007/s10854-025-15113-2).
- 72 P. G. Su and L. Y. Yang, NH<sub>3</sub> gas sensor based on Pd/SnO<sub>2</sub>/RGO ternary composite operated at room-temperature, *Sens. Actuators, B*, 2016, 223, 202, DOI: [10.1016/j.snb.2015.09.091](https://doi.org/10.1016/j.snb.2015.09.091).
- 73 H. Tai, Z. Yuan, W. Zheng, Z. Ye, C. Liu and X. Du, ZnO Nanoparticles/Reduced Graphene Oxide Bilayer Thin Films for Improved NH<sub>3</sub>-Sensing Performances at Room Temperature, *Nanoscale Res. Lett.*, 2016, 11, 130, DOI: [10.1186/s11671-016-1343-7](https://doi.org/10.1186/s11671-016-1343-7).
- 74 Z. Qin, C. Ouyang, J. Zhang, L. Wan, S. Wang, C. Xie and D. Zeng, 2D WS<sub>2</sub> nanosheets with TiO<sub>2</sub> quantum dots decoration for high-performance ammonia gas sensing at room temperature, *Sens. Actuators, B*, 2017, 253, 1034, DOI: [10.1016/j.snb.2017.07.052](https://doi.org/10.1016/j.snb.2017.07.052).
- 75 Y. Chen, W. Zhang and Q. Wu, A highly sensitive room-temperature sensing material for NH<sub>3</sub>: SnO<sub>2</sub>-nanorods coupled by Rgo, *Sens. Actuators, B*, 2017, 242, 1216, DOI: [10.1016/j.snb.2016.09.096](https://doi.org/10.1016/j.snb.2016.09.096).
- 76 R. Li, K. Jiang, S. Chen, Z. Lou, T. Huang, D. Chen and G. Shen, SnO<sub>2</sub>/SnS<sub>2</sub> nanotubes for flexible room-temperature NH<sub>3</sub> gas sensors, *RSC Adv.*, 2017, 7, 52503, DOI: [10.1039/C7RA10537A](https://doi.org/10.1039/C7RA10537A).
- 77 T. Wang, Z. Sun, D. Huang, Z. Yang, Q. Ji, N. Hu, G. Yin, D. He, H. Wei and Y. Zhang, Studies on NH<sub>3</sub> gas sensing by zinc oxide nanowire-reduced graphene oxide nanocomposites, *Sens. Actuators, B*, 2017, 252, 284, DOI: [10.1016/j.snb.2017.05.162](https://doi.org/10.1016/j.snb.2017.05.162).
- 78 P. Kaushik, M. Elias, J. Prasek, Z. Pytlecek and L. Zajickova, Titanium Dioxide Modified Multi-Walled Carbon Nanotubes as Room Temperature NH<sub>3</sub> Gas Sensors, *Proc. IEEE Sens.*, 2018, 7, 1–3, DOI: [10.1109/ICSENS.2018.8589876](https://doi.org/10.1109/ICSENS.2018.8589876).
- 79 Y. Seekaew, W. Pon-On and C. Wongchoosuk, Ultrahigh Selective Room-Temperature Ammonia Gas Sensor Based on Tin-Titanium Dioxide/reduced Graphene/Carbon Nanotube Nanocomposites by the Solvothermal Method, *ACS Omega*, 2019, 4(16), 16916, DOI: [10.1021/acsomega.9b02185](https://doi.org/10.1021/acsomega.9b02185).
- 80 M. M. Sivalingam, J. A. Olmos-Asar, E. Vinoth, T. Tharmar, M. Shkir, Z. Said and K. Balasubramanian, Copper Oxide Nanorod/Reduced Graphene Oxide Composites for NH<sub>3</sub>



- Sensing, *Nano Mater.*, 2021, **4**(12), 12977, DOI: [10.1021/acsnm.1c01831](https://doi.org/10.1021/acsnm.1c01831).
- 81 A. N. Begi, S. Hussain, M. J. Liaqat, N. S. Alsaiani, M. Ouladsmame, G. Qiao and G. Liu, Unlocking low-concentration NH<sub>3</sub> gas sensing: An innovative MOF-derived In<sub>2</sub>O<sub>3</sub>/Co<sub>3</sub>O<sub>4</sub> nanocomposite approach, *Mater. Sci. Semicond. Process.*, 2024, **181**, 108641, DOI: [10.1016/j.mssp.2024.108641](https://doi.org/10.1016/j.mssp.2024.108641).
- 82 H. M. Ragab, N. S. Diab, G. M. Aleid, R. A. Aziz, M. O. Farea, N. Yusof and M. A. Farea, Enhanced detection of ammonia (NH<sub>3</sub>) using a TiO<sub>2</sub>/PANI/GO composite for real-time environmental monitoring, *Chem. Phys. Lett.*, 2025, **869**, 142044, DOI: [10.1016/j.cplett.2025.142044](https://doi.org/10.1016/j.cplett.2025.142044).
- 83 Z. Wu, Z. Chen, Z. Deng, N. Dai, Y. Sun and M. Ge, A high-performance room-temperature NH<sub>3</sub> gas sensor based on WO<sub>3</sub>/TiO<sub>2</sub> nanocrystals decorated with Pt NPs, *RSC Adv.*, 2024, **14**, 12225, DOI: [10.1039/d4ra00881b](https://doi.org/10.1039/d4ra00881b).
- 84 Xu. Cheng, Y. Liu, W. Zhong, S. Li, Y. Li, Z. Zhao, C. Zhang, J. Shi, H. Liu, Z. Zhu and F. Xu, An Ultra-Selective and Humidity-Resistant Room-Temperature-Operated NO<sub>2</sub> Sensor Based on Black TiO<sub>2</sub>, *Adv. Sci.*, 2025, **12**(41), e09293, DOI: [10.1002/advs.202509293](https://doi.org/10.1002/advs.202509293).
- 85 X. Li, Y. Zhao, X. Wang, J. Wang, A. M. Gaskov and S. A. Akbar, Reduced graphene oxide (rGO) decorated TiO<sub>2</sub> microspheres for selective room-temperature gas sensors, *Sens. Actuators, B*, 2016, **230**, 330, DOI: [10.1016/j.snb.2016.02.069](https://doi.org/10.1016/j.snb.2016.02.069).
- 86 H. J. Kim and J. H. Lee, Highly sensitive and selective gas sensors using p-type oxide semiconductors: Overview, *Sens. Actuators, B*, 2014, **192**, 607, DOI: [10.1016/j.snb.2013.11.005](https://doi.org/10.1016/j.snb.2013.11.005).
- 87 M. D. Fernández-Ramosa, L. F. Capitán-Vallveya, L. M. Pastrana-Martínez, S. Morales-Torres and F. J. Maldonado-Hódar, Chemoresistive NH<sub>3</sub> gas sensor at room temperature based on the carbon gel-TiO<sub>2</sub> nanocomposites, *Sens. Actuators, B*, 2022, **368**, 132103, DOI: [10.1016/j.snb.2022.132103](https://doi.org/10.1016/j.snb.2022.132103).
- 88 Z. Ye, H. Tai, T. Xie, Y. Su, Z. Yuan, C. Liu and Y. Jiang, A facile method to develop novel TiO<sub>2</sub>/rGO layered film sensor for detecting ammonia at room temperature, *Mater. Lett.*, 2016, **165**, 127, DOI: [10.1016/j.matlet.2015.11.129](https://doi.org/10.1016/j.matlet.2015.11.129).

